

## Synthesis of Open-Shell, Bimetallic Mn/Fe Trinuclear Clusters

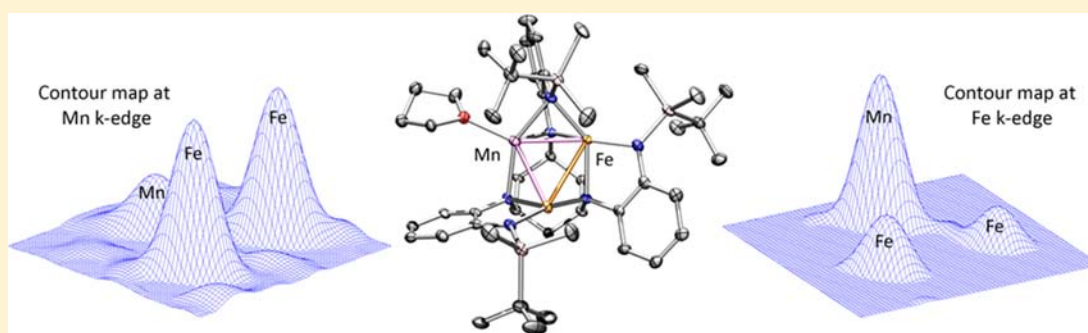
Tamara M. Powers,<sup>†</sup> Nina X. Gu,<sup>†</sup> Alison R. Fout,<sup>‡</sup> Anne M. Baldwin,<sup>†</sup> Raúl Hernández Sánchez,<sup>†</sup> Denise M. Alfonso,<sup>†</sup> Yu-Sheng Chen,<sup>§</sup> Shao-Liang Zheng,<sup>†</sup> and Theodore A. Betley<sup>\*,†</sup>

<sup>†</sup>Department of Chemistry and Chemical Biology, Harvard University, 12 Oxford Street, Cambridge, Massachusetts 02138, United States

<sup>‡</sup>Department of Chemistry, University of Illinois, 600 South Mathews Avenue, Urbana, Illinois 61801, United States

<sup>§</sup>ChemMatCARS, The University of Chicago, Argonne, Illinois 60439, United States

### Supporting Information



**ABSTRACT:** Concomitant deprotonation and metalation of hexadentate ligand platform <sup>tbs</sup>LH<sub>6</sub> (<sup>tbs</sup>LH<sub>6</sub> = 1,3,5-C<sub>6</sub>H<sub>9</sub>(NHC<sub>6</sub>H<sub>4</sub>-*o*-NHSiMe<sub>2</sub><sup>t</sup>Bu)<sub>3</sub>) with divalent transition metal starting materials Fe<sub>2</sub>(Mes)<sub>4</sub> (Mes = mesityl) or Mn<sub>3</sub>(Mes)<sub>6</sub> in the presence of tetrahydrofuran (THF) resulted in isolation of homotrimeric complexes (<sup>tbs</sup>L)Fe<sub>3</sub>(THF) and (<sup>tbs</sup>L)Mn<sub>3</sub>(THF), respectively. In the absence of coordinating solvent (THF), the deprotonation and metalation exclusively afforded dinuclear complexes of the type (<sup>tbs</sup>LH<sub>2</sub>)M<sub>2</sub> (M = Fe or Mn). The resulting dinuclear species were utilized as synthons to prepare bimetallic trinuclear clusters. Treatment of (<sup>tbs</sup>LH<sub>2</sub>)Fe<sub>2</sub> complex with divalent Mn source (Mn<sub>2</sub>(N(SiMe<sub>3</sub>)<sub>2</sub>)<sub>4</sub>) afforded the bimetallic complex (<sup>tbs</sup>L)Fe<sub>2</sub>Mn(THF), which established the ability of hexamine ligand <sup>tbs</sup>LH<sub>6</sub> to support mixed metal clusters. The substitutional homogeneity of (<sup>tbs</sup>L)Fe<sub>2</sub>Mn(THF) was determined by <sup>1</sup>H NMR, <sup>57</sup>Fe Mössbauer, and X-ray fluorescence. Anomalous scattering measurements were critical for the unambiguous assignment of the trinuclear core composition. Heating a solution of (<sup>tbs</sup>LH<sub>2</sub>)Mn<sub>2</sub> with a stoichiometric amount of Fe<sub>2</sub>(Mes)<sub>4</sub> (0.5 mol equiv) affords a mixture of both (<sup>tbs</sup>L)Mn<sub>2</sub>Fe(THF) and (<sup>tbs</sup>L)Fe<sub>2</sub>Mn(THF) as a result of the thermodynamic preference for heavier metal substitution within the hexa-anilido ligand framework. These results demonstrate for the first time the assembly of mixed metal cluster synthesis in an unbiased ligand platform.

### 1. INTRODUCTION

Metal atom substitution within a polynuclear reaction site can have dramatic effects in the local electronic structure resulting in changes in observed reactivity, substrate binding affinities, and catalytic function. Metal atom substitution as a design principle provides a powerful means for altering reaction chemistry without changing the supporting ligand environment. In biology this is observed where metal substitution in Fe-only nitrogenase to FeMo- and FeV-based nitrogenase results in significant changes in enzymatic activity and chemoselectivity (Figure 1a),<sup>1</sup> whereas substitution of a single Fe center in ribonucleotide reductase (RNR) with Mn changes the mechanism of radical initiation (Figure 1b).<sup>2</sup> This phenomenon is not limited to biology as alloys are frequently utilized in industrial heterogeneous catalysis and in some cases demonstrate vastly different catalytic properties and activity relative to the pure metal surface counterparts.<sup>3</sup> For example, long chain

hydrocarbons are generated industrially by the Fischer–Tropsch process, which utilizes bimetallic surfaces including Fe/Co, Co/Ni, and Ni/Fe alloys.<sup>3g,h</sup> While the utility of metal atom substitution to alter reaction chemistry is clear from biological and heterogeneous catalysis, the exact role that metal substitution plays in these polynuclear reaction sites is difficult to assess. Indeed, a synthetic platform wherein multiple combinations of transition or main group atoms could be substituted into an unbiased ligand framework would help illuminate the underlying factors that lead to desirable chemistry.

For the aforementioned reasons, synthetic, heterometallic clusters have been pursued to probe the effect of metal substitution on cluster reactivity, as well as gain a better

Received: August 2, 2013

Published: August 28, 2013

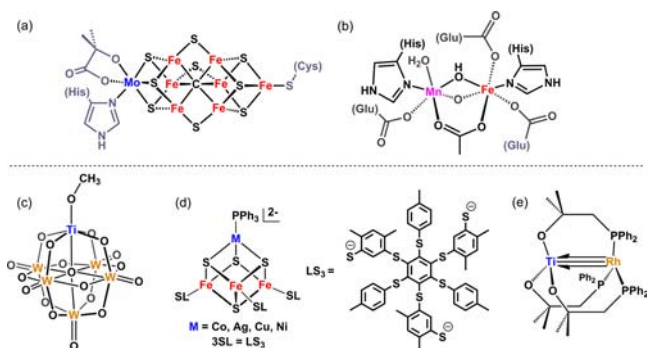


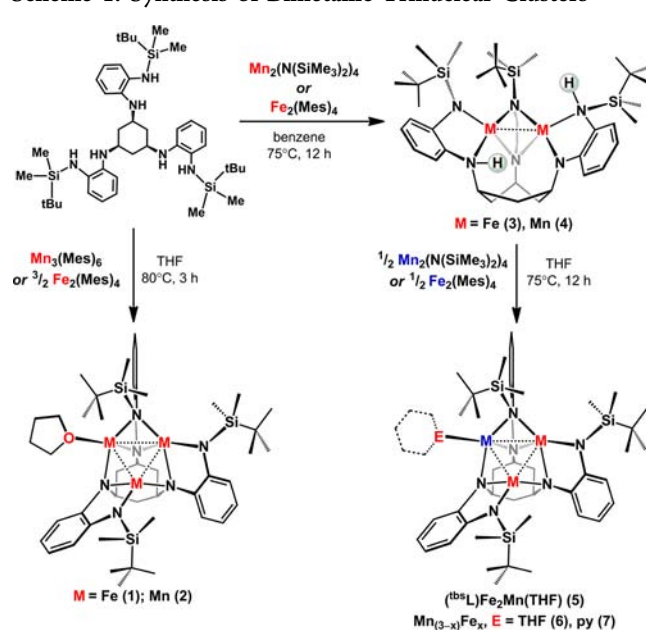
**Figure 1.** Bimetallic metalloenzymes: (a) FeMoco<sup>1</sup> and (b) Fe<sup>III</sup>Mn<sup>IV</sup> of ribonucleotide reductase;<sup>2b</sup> and bimetallic compounds accessed by (c) self-assembly methods (e.g., polyoxometalates),<sup>4</sup> (d) reaction of incomplete cuboidal Fe<sub>3</sub>S<sub>4</sub> clusters,<sup>5</sup> and (e) polynucleating ligands that have different elemental binding affinities.<sup>6</sup>

understanding of the stability, reactivity, and coordination environment of the individual metal reaction sites.<sup>7</sup> Four general strategies have been employed to synthesize mixed-metal clusters: (1) self-assembly processes<sup>4,8</sup> (Figure 1c); (2) reaction of incomplete clusters (e.g., partially formed cubanes) with binary transition metal or alkaline ions<sup>5,9,10</sup> (Figure 1d); (3) utilization of polynucleating ligand scaffolds that possess different elemental binding affinities to selectively interact with one metal ion in preference to another (Figure 1e);<sup>6,11</sup> and (4) direct atom metathesis from preformed clusters.<sup>12</sup> What has not been demonstrated is the straightforward synthesis of polymetallic clusters featuring direct, close M–M interactions in an unbiased ligand environment.

Our lab has approached the synthesis of metal clusters through the development of a family of hexadentate ligand platforms, which provide a method of structure–function analysis through systematic modification of the steric and electronic environment of the cluster. We have previously reported the synthesis of several homotrimeric clusters of Co, Mn, and Fe, supported by hexadentate ligand platforms comprised of *o*-phenylenediamide-based subunits, whose intracore interactions and molecular spin states vary as a function of ligand architecture.<sup>13</sup> Adapting our synthetic protocols to yield bi- or trimetallic trinuclear clusters supported by hexaanilide ligand platforms would provide an alternative avenue by which we can investigate the role M–M interactions play in both cluster electronic structure and reactivity. The synthesis of polynuclear heterometallic clusters supported by polynucleating ligand scaffolds that feature unbiased metal-binding sites has not yet been realized, potentially due to the challenge of controlling the number and sites of metal incorporation.

Recently, we reported the synthesis of cluster (<sup>tbs</sup>L)-Fe<sub>3</sub>(THF) (1) (<sup>tbs</sup>L<sup>6-</sup> = [1,3,5-C<sub>6</sub>H<sub>9</sub>(NC<sub>6</sub>H<sub>4</sub>-*o*-NSiMe<sub>2</sub><sup>t</sup>Bu)<sub>3</sub>]<sup>6-</sup>).<sup>14</sup> In the absence of coordinating solvent, we access binuclear metal complexes (<sup>tbs</sup>LH<sub>2</sub>)M<sub>2</sub>, providing a platform by which we can explore the stepwise synthesis of a family of mixed-metal clusters that differ by single metal-site substitutions (Scheme 1). Through this investigation we have sought to address the following questions: (1) Can the hexaanilide ligand (<sup>tbs</sup>L<sup>6-</sup>) support all metal substitution combinations from Mn<sub>3</sub> to Fe<sub>3</sub> in single metal-substitution steps? (2) Are substitutionally homogeneous clusters formed upon metalation (i.e., same metal occupancy and position within the ligand framework), or does metal atom lability

## Scheme 1. Synthesis of Bimetallic Trinuclear Clusters



produce statistical distributions of mixed-metal compositions? (3) Can ancillary ligands, such as coordinated solvent molecules (THF in Scheme 1), be used to tune the selectivity of metal substitution reaction?

## 2. EXPERIMENTAL SECTION

**2.1. Materials and Methods.** All manipulations involving metal complexes were carried out using standard Schlenk line or glovebox techniques under a dinitrogen atmosphere. All glassware was oven-dried for a minimum of 10 h and cooled in an evacuated antechamber prior to use in the drybox. Benzene, diethyl ether, hexanes and tetrahydrofuran (THF) were dried and deoxygenated on a Glass Contour System (SG Water USA, Nashua, NH) and stored over 4 Å molecular sieves (Strem) prior to use. Benzene-*d*<sub>6</sub> was purchased from Cambridge Isotope Laboratories and was degassed and stored over 4 Å molecular sieves prior to use. Nonhalogenated solvents were typically tested with a purple solution of sodium benzophenone ketyl in THF in order to confirm effective oxygen and moisture removal. <sup>tbs</sup>LH<sub>6</sub>,<sup>14</sup> Fe<sub>2</sub>Mes<sub>4</sub> (Mes = 2,4,6-Me<sub>3</sub>C<sub>6</sub>H<sub>2</sub>),<sup>15</sup> Mn<sub>3</sub>(Mes)<sub>6</sub>,<sup>16</sup> and Mn<sub>2</sub>(NSi(CH<sub>3</sub>)<sub>3</sub>)<sub>4</sub><sup>17</sup> were prepared following published methods. All other reagents were purchased from commercial vendors and used without further purification.

All of the measurements for the metal complexes, except for X-ray fluorescence spectroscopy, were made under anaerobic conditions. Elemental analyses were performed by Complete Analysis Laboratories, Inc., Parsippany, NJ. <sup>1</sup>H NMR spectra were recorded on Varian Unity/Inova 500B/600 NMR spectrometers with chemical shifts ( $\delta$  ppm) referenced to residual NMR solvent (C<sub>6</sub>D<sub>6</sub>, 7.16 ppm). Perpendicular and parallel mode X-band EPR spectra were recorded on Bruker ElexSys E500 EPR (fitted with a cryostat for measurements at 4 K). The EPR spectra were referenced to diphenylpicrylhydrazyl (DPPH;  $g = 2.0037$ ).

**2.2. Synthesis.** (<sup>tbs</sup>L)Mn<sub>3</sub>(THF) (2). <sup>tbs</sup>LH<sub>6</sub> (0.300 g, 0.403 mmol) and Mn<sub>3</sub>(Mes)<sub>6</sub> (0.366 g, 0.416 mmol) were each dissolved in 2 mL of benzene. The Mn<sub>3</sub>(Mes)<sub>6</sub> solution was then added to the <sup>tbs</sup>LH<sub>6</sub> solution at 23 °C followed by the addition of THF (1 mL) to the reaction mixture. The reaction was heated in a sealed bomb at 80 °C for 3 h. The volatiles were removed in vacuo, followed by lyophilization from benzene to afford a brown solid. The resulting material was dissolved in hexanes (20 mL) and filtered through Celite on a medium porosity fritted funnel. The filtrate was dried in vacuo to afford the title complex as a reddish-brown solid. The product is <sup>1</sup>H NMR silent. X-ray quality crystals were grown from cold hexanes (–33

°C). Isolated yield: 0.323, (84%). Anal. Calcd for  $C_{46}H_{74}Mn_3N_6OSi_3$ : C 56.60, H 7.64, N 8.61. Found: C 56.47, H 7.65, N 8.53.

$(^{tbs}LH_2)Fe_2$  (**3**). Solid  $^{tbs}LH_6$  (0.130 g, 0.174 mmol) was dissolved in 10 mL of benzene. The solution was added to solid  $Fe_2(Mes)_4$  (0.129 g, 0.218 mmol) at 23 °C. The mixture was heated in a sealed reaction vessel at 75 °C for 12 h. The volatiles were removed in vacuo, followed by lyophilization from benzene, and the residue was washed with 5 mL of cold hexanes (−33 °C) to afford the title complex as a brown solid. Compound **3** is stable as a solid at −33 °C for at least 2 weeks. X-ray quality crystals were grown from cold hexanes (−33 °C). Isolated yield: 0.092 g (62%).  $^1H$  NMR (benzene- $d_6$ , 500 MHz,  $\delta$ , ppm): 82.9, 52.3, 39.2, 37.7, 32.8, 25.0, 24.4, 23.2, 22.2, 20.1, 19.5, 14.5, 14.2, 12.9, 11.9, −2.31, −5.70, −15.2, −24.7, −32.2, −32.9, −34.0, −40.7; Anal. Calcd for  $C_{50}H_{71}Fe_3LiN_6Si_3$ : C 59.14, H 8.04, N 9.85. Found: C 59.07, H 7.98, N 9.74; Zero-field  $^{57}Fe$  Mössbauer (90 K) ( $\delta$ ,  $|dE_Q|$  (mm/s)): component 1 (39%): 0.67, 2.19 ( $\Gamma = 0.17$  mm/s); component 2 (61%): 0.68, 1.60 ( $\Gamma = 0.28$  mm/s); UV–vis Spectroscopy (THF): 262 nm ( $\epsilon = 1.98 \times 10^5$  M $^{-1}cm^{-1}$ ); 290 nm ( $\epsilon = 1.40 \times 10^5$  M $^{-1}cm^{-1}$ ); 334 nm ( $\epsilon = 7.45 \times 10^4$  M $^{-1}cm^{-1}$ ); 455 nm ( $\epsilon = 1.49 \times 10^5$  M $^{-1}cm^{-1}$ ).

$(^{tbs}LH_2)Mn_2$  (**4**). Solid  $^{tbs}LH_6$  (0.160 g, 0.215 mmol) was dissolved in 10 mL of benzene. The solution was added to solid  $Mn_2(N(SiMe_3)_2)_4$  (0.192 g, 0.256 mmol) at 23 °C. The reaction was heated in a sealed bomb at 75 °C for 12 h. The volatiles were removed in vacuo, followed by lyophilization from benzene, and the residue was dissolved in 10 mL of hexanes. The hexane solution was filtered through Celite and the volatiles were removed in vacuo to afford the title complex as a tan solid. Complex **4** is  $^1H$  NMR silent. X-ray quality crystals were grown from cold hexanes (−33 °C). Isolated yield: 0.128 g (70%). Anal. Calcd for  $C_{42}H_{68}Mn_2N_6Si_3$ : C 59.27, H 8.05, N 9.87. Found: C 59.13, H 7.95, N 9.79.

$(^{tbs}L)Fe_2Mn(THF)$  (**5**). Solid  $(^{tbs}LH_2)Fe_2$  (**3**) (0.060 g, 0.070 mmol) was dissolved in 5 mL of THF. The solution was added to solid  $Mn_2(N(SiMe_3)_2)_4$  (0.026 g, 0.035 mmol) at 23 °C and the resulting mixture was heated at 75 °C for 12 h. The volatiles were removed in vacuo and dissolved in approximately 3 mL of hexanes. The hexanes were removed in vacuo to afford a brown solid. Isolated yield: 0.043 g (62%). Crystalline material was isolated from a diethyl ether solution at −33 °C. Crystalline yield: 0.023 g (33%).  $^1H$  NMR (benzene- $d_6$ , 500 MHz,  $\delta$ , ppm): 285.4, 262.3, 129.8, 74.27, 52.38, 48.60, 43.15, 37.38, 35.62, 30.43, 24.20, 20.61, 18.13, 10.83, 9.38, 5.82, 5.09, 2.78, 2.07, 1.20, 0.06, −1.07, −1.66, −3.63, −9.47, −12.28, −12.31, −26.74, −33.05, −38.83, −56.99, −82.97; Anal. Calcd for  $C_{46}H_{74}Fe_2MnN_6OSi_3$ : C 56.49, H 7.63, N 8.59. Found: C 56.37, H 7.61, N 8.47; Zero-field  $^{57}Fe$  Mössbauer (90 K) ( $\delta$ ,  $|dE_Q|$  (mm/s)): component 1 (48%): 0.35, 1.77 ( $\Gamma = 0.20$  mm/s); component 2 (52%): 0.58, 1.30 ( $\Gamma = 0.22$  mm/s).

**Reaction of 4 with  $Fe_2(Mes)_4$  (**6**)**. Solid  $(^{tbs}LH_2)Mn_2$  (**4**) (0.060 g, 0.070 mmol) was dissolved in 5 mL of THF. The solution was added to solid  $Fe_2(Mes)_4$  (0.023 g, 0.039 mmol) at 23 °C. The reaction was heated at 75 °C for 12 h. The volatiles were removed in vacuo and the residue was washed with approximately 1 mL of hexanes. The remaining brown solid was dissolved in diethyl ether (~2 mL). Crystalline material was isolated from the diethyl ether solution at −33 °C. Crystalline yield: 0.010 g (14%).  $^1H$  NMR (benzene- $d_6$ , 500 MHz,  $\delta$ , ppm): 187.6, 182.6, 129.8, 117.3, 74.33, 55.73, 52.4, 48.62, 47.19, 43.19, 41.73, 37.44, 35.66, 31.75, 30.47, 28.99, 24.26, 21.41, 20.73, 18.17, 10.87, 9.42, 6.73, 5.86, 5.14, 4.30, 3.31, 2.81, 2.40, 2.16, 0.30, 0.10, −1.00, −1.63, −3.61, −5.96, −9.44, −10.03, −11.76, −12.24, −15.79, −20.79, −24.52, −26.72, −32.95, −36.53, −38.80, −56.94, −82.98; Anal. Calcd for  $C_{46}H_{74}FeMn_2N_6Si_3O$ : C 56.54, H 7.63, N 8.60. Found: C 56.48, H 7.67, N 8.54; Zero-field  $^{57}Fe$  Mössbauer (90 K) ( $\delta$ ,  $|dE_Q|$  (mm/s)): component 1 (48%): 0.33, 1.85 ( $\Gamma = 0.14$  mm/s); component 2 (52%): 0.57, 1.31 ( $\Gamma = 0.19$  mm/s).

**Reaction of 4 with  $Fe_2(Mes)_4$  and Pyridine (**7**)**. Solid  $Fe_2(Mes)_4$  (0.023 g, 0.039 mmol) was dissolved in 3 mL of benzene at 23 °C. Pyridine (py; ~15  $\mu$ L) was added to the  $Fe_2(Mes)_4$  solution followed by addition of a solution of  $(^{tbs}LH_2)Mn_2$  (**4**) (0.060 g, 0.070 mmol) in benzene (2 mL). The resulting mixture was heated at 75 °C for 12 h. The volatiles were removed in vacuo and the residue was washed with

approximately 1 mL of hexanes. The remaining brown solid was dissolved in diethyl ether (1–2 mL). Crystalline material was isolated from the diethyl ether solution at −33 °C. Crystalline yield: 0.022 g (31%).  $^1H$  NMR (benzene- $d_6$ , 500 MHz,  $\delta$ , ppm): 185.5, 172.5, 128.4, 116.0, 72.41, 54.02, 53.20, 48.10, 47.28, 46.54, 42.62, 39.73, 34.18, 31.94, 28.74, 25.63, 23.44, 22.18, 19.90, 18.51, 11.10, 11.10, 9.77, 6.69, 3.23, 2.92, 2.18, 2.12, 0.93, 0.14, −0.27, −1.45, −2.19, −3.87, −6.34, −7.60, −9.99, −11.23, −12.01, −14.10, −17.32, −20.98, −22.31, −23.92, −25.90, −30.86, −35.48, −37.87, −55.08, −81.72; Anal. Calcd for  $C_{47}H_{71}FeMn_2N_7Si_3$ : C 57.36, H 7.27, N 9.96. Found: C 57.43, H 7.20, N 9.78; Zero-field  $^{57}Fe$  Mössbauer (90 K) ( $\delta$ ,  $|dE_Q|$  (mm/s)): component 1 (54%): 0.33, 1.85 ( $\Gamma = 0.17$  mm/s); component 2 (46%): 0.57, 1.24 ( $\Gamma = 0.19$  mm/s).

**2.3. X-Ray Diffraction Techniques.** All structures were collected on a Bruker three-circle platform goniometer equipped with an Apex II CCD and an Oxford cryostream cooling device at 100 K. Radiation for the data collection of **2**, **3**, and **4** was from a graphite fine focus sealed tube Mo  $K\alpha$  (0.71073 Å) source. All other structures were obtained using radiation from a synchrotron source (0.44280 Å or 0.49594 Å). Crystals were mounted on a cryoloop or glass fiber pin using Paratone-N oil. Data were collected as a series of  $\varphi$  and/or  $\omega$  scans. Data were integrated using SAINT<sup>18</sup> and scaled with either a numerical or multiscan absorption correction using SADABS.<sup>18</sup> The structures were solved by direct methods or Patterson maps using SHELXS-97 and refined against  $F^2$  on all data by full matrix least-squares with SHELXL-97.<sup>19</sup> All non-hydrogen atoms were refined anisotropically. Hydrogen atoms were placed at idealized positions and refined using a riding model. The isotropic displacement parameters of all hydrogen atoms were fixed to 1.2 times the atoms they are linked to (1.5 times for methyl groups). Further details on particular structures are noted in the Supporting Information.

**2.4. Mössbauer Spectroscopy.** Zero-field,  $^{57}Fe$  Mössbauer spectra were measured with a constant acceleration spectrometer (SEE Co, Minneapolis, MN). Crystalline samples were prepared as Paratone-N mulls in a glovebox and frozen in liquid nitrogen prior to handling in air. Isomer shifts are quoted relative to Fe metal at 23 °C. Data was processed, simulated, and analyzed using an in-house package for IGOR Pro 6 (Wavemetrics, Lake Oswego, OR).

**2.5. X-ray fluorescence.** X-ray fluorescence analyses were recorded on a Bruker Tracer III-SD XRF analyzer with no additional filter and data was collected on each sample for at least 10 min. Samples for the calibration curve were prepared by dissolving iron(III) chloride and manganese(II) chloride tetrahydrate in water. The  $K\alpha$  and  $K\beta$  of pure Fe and Mn were each fit to a Gaussian line shape. The calibration samples were fit to three Gaussian lineshapes representing the Mn  $K\alpha$  emission, the overlapping Mn  $K\beta$  and Fe  $K\alpha$  emissions, and the Fe  $K\beta$  emission. The area of the Mn  $K\beta$  emission was calculated using the area of the Gaussian fit of the Mn  $K\alpha$  emission and the Mn  $K\alpha$  and  $K\beta$  ratio of the areas of a pure sample manganese(II)chloride tetrahydrate. Quantification was performed using the sum of the  $K\alpha$  and  $K\beta$  areas. Fe:Mn ratios in samples were determined from the peak area ratios using the linear fit to the calibration curve (Supporting Information Figure S9).

**2.6. Anomalous X-Ray Diffraction Techniques.** All anomalous X-ray diffraction data were collected at ChemMatCARS at the Advanced Photon Source at Argonne National Laboratory (CARS, Center for Advanced Radiation Sources). The data were collected on a Bruker D8 diffractometer equipped with an APEX II CCD at 100 K using Cyrojet (Oxford instrumentation). Anomalous X-ray diffraction data was collected at wavelengths at the elemental absorption K-edges of Mn (6.539 keV) and Fe (7.112 keV). In some cases, data was collected between 30–50 eV above and/or below the Mn and Fe K-edges. Data was integrated using SAINT and scaled with either a numerical or multiscan absorption correction using SADABS.<sup>18</sup> Structure factors  $f'$  and  $f''$  were determined for a given wavelength based on theoretical values<sup>20</sup> from the XDISP function in the WINGX<sup>21</sup> program unless otherwise noted. Anomalous difference Fourier electron density maps at the absorption edges were also generated using SHELXL-97<sup>19</sup> and WINGX,<sup>21</sup> by fixed refinement of the atomic model generated by the reference data set (1a or 1b) with



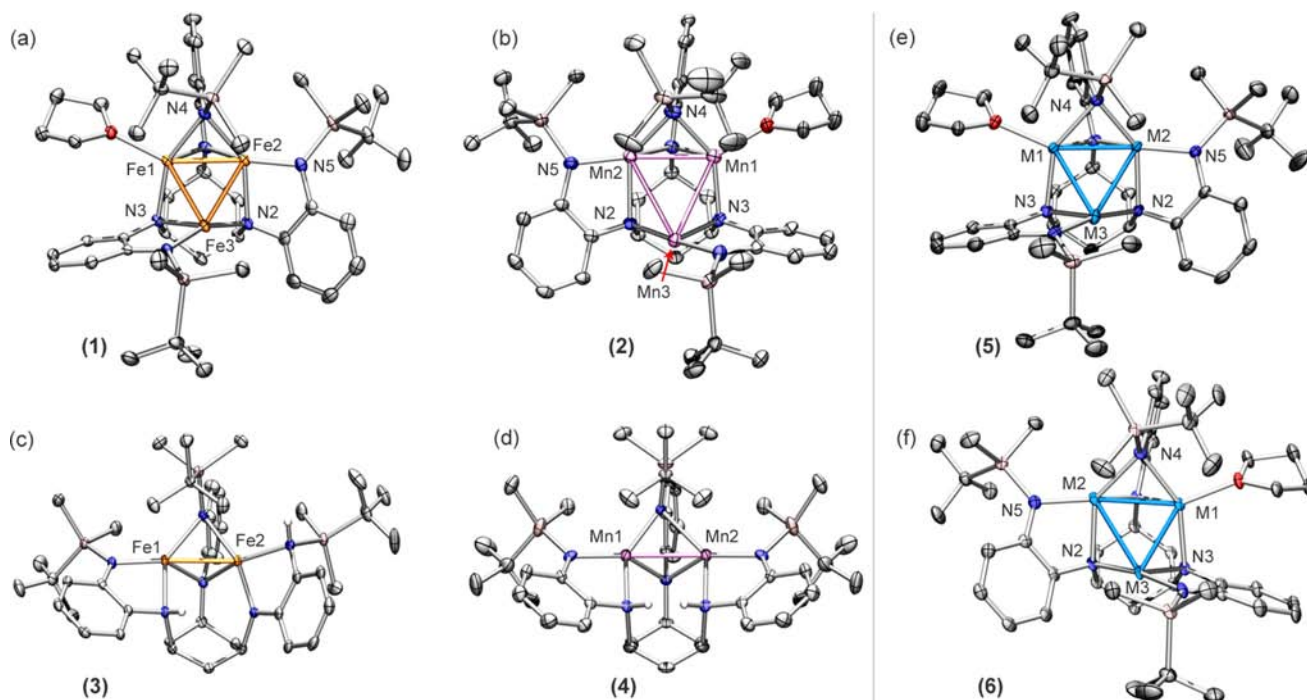


**Figure 2.** Solid-state structures for (a)  $(\text{tbsL})\text{Fe}_3(\text{THF})$  (1), (b)  $(\text{tbsL})\text{Mn}_3(\text{THF})$  (2), (c)  $(\text{tbsLH}_2)\text{Fe}_2$  (3), (d)  $(\text{tbsLH}_2)\text{Mn}_2$  (4) with the thermal ellipsoids set at 50% probability level (hydrogen atoms and solvent molecules omitted for clarity; Fe orange, Mn orchid, N blue, O red, C gray, H white, Si pink). Solid state structures for bimetallic trinuclear compounds (e)  $(\text{tbsL})\text{M}_3(\text{THF})$  (5) and (f)  $(\text{tbsL})\text{M}_3(\text{THF})$  (6) with the thermal ellipsoids set at 50% probability level. The identity of the metal centers could not be determined using traditional X-ray crystallographic methods and therefore all metal centers are depicted as light blue.

the reflection data obtained at the metal absorption edge. The electron density holes measured in  $e^-/\text{\AA}^3$  were determined by looking at the 2D electron density maps in MCE.<sup>22</sup> The percent occupancies of Fe and Mn at each metal position were refined using SHELXL-97<sup>19</sup> as described by Helliwell et al.<sup>23</sup> When refining the metal occupancies near and at the metal absorption edges, the metal positions were fixed using the EXYZ restraint unless otherwise noted.

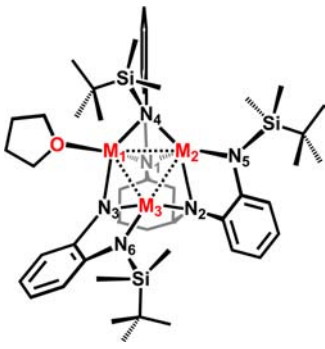
### 3. RESULTS

Herein, we present the synthesis of homotrimeric  $(\text{tbsL})\text{Fe}_3(\text{THF})$  (1) and  $(\text{tbsL})\text{Mn}_3(\text{THF})$  (2), homodimeric  $(\text{tbsLH}_2)\text{Fe}_2$  (3) and  $(\text{tbsLH}_2)\text{Mn}_2$  (4), and the bimetallic trinuclear  $(\text{tbsL})\text{Fe}_2\text{Mn}(\text{THF})$  (5) complexes supported within a hexaanilido ligand. Spectroscopic and structural characterization establishes that these compounds are substitutionally homogeneous materials. Synthetic attempts to prepare the analogous  $(\text{tbsL})\text{Mn}_2\text{Fe}(\text{E})$  complexes (6 and 7, which differ by the coordinated solvent molecule,  $E = \text{THF}$  or  $\text{py}$ , respectively, Scheme 1) resulted in a mixture of bimetallic trinuclear complexes. In section 3.1, we describe the spectral and structural data of 5 and THF ligated mixed-metal complex 6, which was used to assign the metal substitution patterns. In section 3.2, we present anomalous scattering measurements of all three mixed-metal species (5, 6, and 7), providing single-site elemental analysis of the metal positions.

**3.1. Synthesis and bulk spectroscopic characterization.** Metalation of the hexaanilido ligand scaffold 1,3,5- $\text{C}_6\text{H}_3(\text{NHC}_6\text{H}_4\text{-}o\text{-NHSi}^t\text{BuMe}_2)_3$  ( $\text{tbsLH}_6$ ) was effected using 1.5 equivalents of  $\text{Fe}_2(\text{Mes})_4$  or 1 equivalent of  $\text{Mn}_3(\text{Mes})_6$ ;  $\text{Mes} = 2,4,6\text{-Me}_3\text{C}_6\text{H}_2$ , in the presence of tetrahydrofuran (THF) to yield  $(\text{tbsL})\text{Fe}_3(\text{THF})$  (1)<sup>14</sup> and  $(\text{tbsL})\text{Mn}_3(\text{THF})$  (2, 49%), respectively. Crystallographic analysis of single crystals of  $\text{Mn}_3$  cluster 2 shows that the three Mn atoms each possess

unique coordination environments (Figure 2b), identical to those found in previously reported  $\text{Fe}_3$  cluster 1 (Figure 2a). While all three internal alkyl aryl anilides bridge two adjacent metal centers, only one of the peripheral silylanilide ligands bridges Mn1 and Mn2. The remaining two silylanilides are terminally bound to Mn2 and Mn3. The average Mn–Mn distance (3.0730(9) Å) as well as the average Mn– $\text{N}_{\text{Si}}$  (2.042(2) Å) and Mn– $\text{N}_{\text{int}}$  (2.0645(2) Å) distances in 2 are longer than the average Fe–Fe (2.577(6) Å), Fe– $\text{N}_{\text{Si}}$  (1.950(2) Å) and Fe– $\text{N}_{\text{int}}$  (2.047(2) Å) distances in 1 (Table 1).

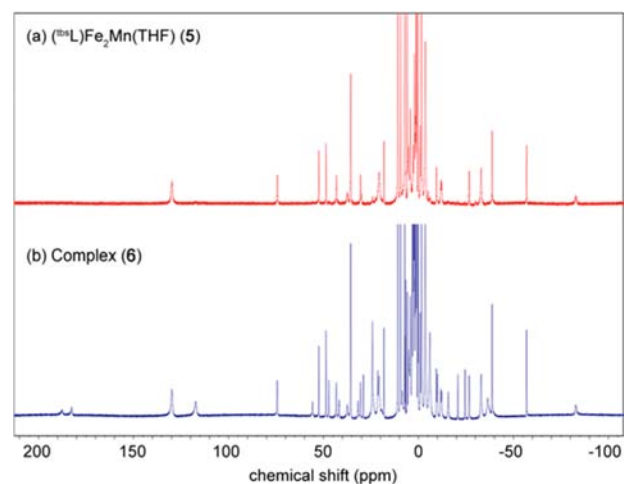
In the absence of coordinating solvent, concomitant deprotonation and metalation of  $\text{tbsLH}_6$  with  $\text{Fe}_2(\text{Mes})_4$  or  $\text{Mn}_2(\text{N}(\text{SiMe}_3)_2)_4$  occurs at 75 °C and results in the formation of dinuclear compounds  $(\text{tbsLH}_2)\text{Fe}_2$  (3, 62%) and  $(\text{tbsLH}_2)\text{Mn}_2$  (4, 70%), respectively. Single crystal analysis of complexes 3 and 4 showed that the two metal centers are bridged by one of the three *o*-phenylenedianilide (OPDA) units of the ligand (Figure 2c,d). The remaining two OPDA units are singly deprotonated (protons located in the electron density map) and are bound to one of the two metal centers. The remaining protonated aniline sites create a binding site to support a third divalent metal center. In the case of 3, one of the silyl aryl nitrogens remains protonated, while the second amine is located in the ligand basal position. The structure of compound 4 was solved with a disorder model, one of which is shown in Figure 2d and features both of the basal amines available for deprotonation. While the M–M separation in  $\text{Fe}_2$  complex 3 (2.7086(6) Å) is longer than the M–M distances observed in the homotrimeric  $\text{Fe}_3$  counterpart 2 (Table 1), the mean Mn–Mn distance increases upon insertion of a third metal center ( $\text{Mn}_2$  complex 4: 2.8560(8) Å;  $\text{Mn}_3$  complex 2 (avg): 3.0730(9) Å).

**Table 1.** Select Metal–Metal and Metal–Ligand Bond Lengths for Compounds 1, 2, 5, and 6


bond	1	2	5	6
M1–M2	2.6129(5)	2.8785(7)	2.7247(5)	2.7681(6)
M2–M3	2.6118(5)	3.2213(7)	2.8687(5)	3.0176(6)
M1–M3	2.5061(5)	3.1191(7)	2.7485(5)	2.8030(6)
avg.	2.5769(6)	3.0730(9)	2.7806(6)	2.8629(7)
M1–N1	2.126(2)	2.116(3)	2.148(2)	2.123(2)
M1–N3	2.016(2)	2.077(3)	2.121(2)	2.126(2)
M1–N4	2.081(2)	2.148(3)	2.170(2)	2.158(2)
avg.	2.074(3)	2.114(4)	2.146(3)	2.136(3)
M2–N1	2.047(2)	2.109(3)	2.047(2)	2.079(2)
M2–N2	2.091(2)	2.162(2)	2.108(2)	2.123(2)
M2–N4	2.149(2)	2.202(3)	2.122(2)	2.171(2)
M2–N5	1.950(2)	2.098(3)	1.956(2)	1.985(2)
avg.	2.059(3)	2.143(4)	2.058(3)	2.090(3)
M3–N2	1.955(2)	2.000(3)	1.945(2)	1.935(2)
M3–N3	2.053(2)	2.098(3)	2.018(2)	2.019(2)
M3–N6	1.938(2)	1.976(3)	1.920(2)	1.920(2)
avg.	1.982(3)	2.025(4)	1.961(3)	1.958(3)

The ability to access dinuclear species **3** and **4** is key for accessing bimetallic trinuclear species supported by the ligand variant  $^{tbs}LH_6$ . Importantly, even upon addition of excess divalent Fe or Mn metallating reagent, we never observe formation of a trinuclear species without the presence of coordinating solvent (L = THF or py; see Scheme 1). The role solvent L plays in metalation and/or stabilization of the product is currently unknown. The coordinating solvent could either facilitate breaking down the dimeric metallating agent (e.g.,  $M_2(N(SiMe_3)_2)_4$ ), which may be necessary to generate the trinuclear products, or simply stabilize the resulting trinuclear complex that cannot be supported solely by  $^{tbs}L^{6-}$  in the present oxidation state. If solvent coordination plays a role in stabilizing the trinuclear product, the identity of the coordinating solvent may have an effect on the selectivity of the resulting bimetallic trinuclear clusters.

The synthesis of bimetallic trinuclear cluster  $(^{tbs}L)Fe_2Mn(THF)$  (**5**) was achieved by treatment of the dinuclear Fe complex  $(^{tbs}LH_2)Fe_2$  (**3**) with 0.5 equivalent of  $Mn_2(N(SiMe_3)_2)_4$  in THF at 75 °C (62% isolated yield). Single crystals were obtained from concentrated diethyl ether solutions at –33 °C (33% crystalline yield). The resulting crystalline product has a paramagnetically shifted  $^1H$  NMR spectrum with 32 resonances, consistent with a  $C_1$ -symmetric complex in solution (Figure 3a).  $C_1$ -symmetry is also observed in the solid-state (Figure 2e) where the metal coordination environments in **5** are identical to that of the homotrimeric counterparts **1** and **2** (Figure 2a,b). The average M–M distance of **5** (2.7806(6) Å) is intermediate between the average

**Figure 3.** Paramagnetic  $^1H$  NMR of (a)  $(^{tbs}L)Fe_2Mn(THF)$  **5** (red) and (b) complex **6** (blue).

distances observed for the homotrimeric Fe and Mn complexes (**1**: 2.5769(6) Å; **2**: 3.0730(9) Å) (Table 1). The metal–ligand bond distances for metal centers M2 (2.058(3) Å) and M3 (1.961(3) Å) in **5** are all shorter than or nearly equal to the respective M–N distances found in  $Fe_3$  cluster **1** (2.059(3) Å and 1.982(3) Å, respectively) and the M1–N bond distances (2.146(3) Å) are close to the metal–ligand bond distances in  $Mn_3$  cluster **2** (2.114(3) Å, see Table 1). These bond metrics would suggest that for compound **5**, M1 = Mn and M2 = M3 = Fe, consistent with a site-isolated insertion of a single Mn into **3**. While traditional X-ray crystallography allowed us to establish connectivity, it cannot be used to distinguish the identity of Mn and Fe centers within the cluster. Thus, we used anomalous scattering measurements to rigorously assign the elemental identity of metal sites within the core (*vide infra*).

We approached the synthesis of a  $Mn_2Fe$ -containing cluster in a similar fashion to **5**.  $^1H$  NMR analysis of a solution observed following treatment of  $(^{tbs}LH_2)Mn_2$  (**4**) with 0.5 equivalent of  $Fe_2Mes_4$  at 75 °C displayed more than twice the number of resonances as were observed for **5** (Figure 3b). All of the resonances that account for **5** appear in the  $^1H$  NMR spectrum of **6**, suggesting the  $^1H$  NMR spectrum of **6** represents a mixture of species, one of which is **5** resulting from Fe-for-Mn substitution. For simplicity, the resulting material from the reaction of  $Mn_2$  **4** with 0.5 equiv  $Fe_2(Mes)_4$  will be referred to as compound **6**.

Crystallization of **6** from cold diethyl ether (–33 °C) afforded single crystals that contained a trinuclear species with the same connectivity as observed for homotrimeric complexes **1** and **2** and bimetallic trinuclear complex **5**, with an average M–M distance of 2.8629(7) Å (Figure 2f, Table 1). Based on metal–ligand bond metrics in **6**, it is not clear whether one or two metal types occupy the metal positions. As in the case of **5**, the M1–N bond distances in trinuclear cluster **6** are consistent with those distances observed in homotrimeric  $Mn_3$  cluster **2** (Table 1). Likewise, M3–N bond metrics of **6** suggest that metal position 3 is occupied by Fe (Table 1). However, the M2–N bond lengths for compound **6** do not appear to follow a similar trend and fall between the metal–ligand bond lengths found in the homotrimeric clusters **1** and **2** (Table 1), making it difficult to assign all the metal atom positions.

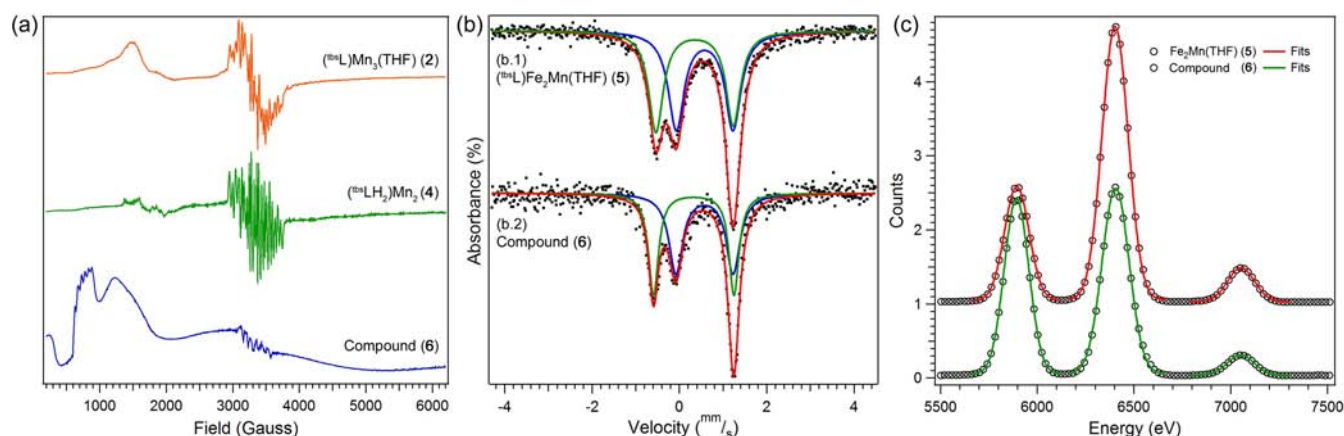


**Figure 4.** (a) EPR of crystalline  $(^{tbs}L)Mn_3(THF)$  (**2**) (orange),  $(^{tbs}LH_2)Mn_2$  (**4**) (green), and bimetallic trinuclear compound (**6**) (blue). (b) Zero-field  $^{57}Fe$  Mössbauer spectra obtained at 90 K of compounds **5** and **6**. Simulation yields the following parameters  $[\delta, |ΔE_Q|]$  (mm/s) for **5**: component 1 (blue 52%) 0.58, 1.30; component 2 (green 48%) 0.35, 1.77; for **6**: component 1 (blue, 52%) 0.57, 1.31; component 2 (green, 48%) 0.33, 1.85. (c) X-ray fluorescence spectra of  $(^{tbs}L)Fe_2Mn(THF)$  (**5**) (red) and complex **6** (green).

EPR spectroscopy was utilized as an additional fingerprint for both the homo and heteronuclear species reported herein. The perpendicular X-band EPR spectra at 4 K for homotrimeric  $Mn_3$  cluster **2** and binuclear  $Mn_2$  cluster **4** exhibit substantial hyperfine coupling at  $g = 2.01$ , due to coupling to the  $I = 5/2$   $^{55}Mn$  nuclei (Figure 4a). Complexes **2** and **4** show spectra exceeding the 16- and 10-line patterns, respectively, expected for hyperfine coupling to equivalent Mn nuclei ( $2nI + 1$ ;  $A_{||} = 29-59$  G for **2** at 4 K;  $A_{||} = 35-64$  G for **4** at 4 K). The multiline hyperfine in the spectra for **2** and **4** is attributed to overlapping 6-line hyperfine patterns, a result of inequivalent Mn environments present in both complexes. The transition centered at  $g = 4.43$  (compound **2**) likely corresponds to a spin-allowed transition associated with the  $m_s = \pm 3/2$  excited state of Mn ( $S = 5/2$ ) and has been observed in X-band EPR spectrum of previously reported  $Mn_3$  clusters.<sup>13b,24</sup> A similar transition can be observed for **4** at  $g = 4.04$  and features hyperfine coupling to the  $I = 5/2$   $^{55}Mn$  nucleus ( $A_{||} = 29-35$  G at 4 K).<sup>25</sup>

Like the  $Mn_3$  (**2**) and  $Mn_2$  (**4**) complexes, compound **6** also exhibits an X-band EPR spectrum at 4 K with hyperfine coupling near  $g = 2$  ( $A_{||} = 64-88$  G at 4 K) (Figure 4a). Compound **6** exhibits two additional features at  $g = 8.91$  ( $A_{||} = 53$  G at 4 K), likely corresponding to spin-allowed transitions associated with the  $m_s = \pm 1/2$  excited state of  $S = 5/2$  Mn ion, as well as a spin forbidden transition at  $g = 15.43$ . While the hyperfine coupling observed in the EPR spectrum of **6** confirms the presence of a  $[Mn_2]$  unit in the resulting crystalline material, it is difficult to ascertain the amount of material that is responsible for the signatures attributed to that unit.<sup>26</sup>

Zero-field  $^{57}Fe$  Mössbauer was used to determine the number of inequivalent iron sites in bimetallic trinuclear clusters **5** and **6**. Table 2 summarizes the Mössbauer parameters after fitting the spectra of the iron containing compounds **1**, **3**, **5**, and **6**. Mixed-metal compounds **5** and **6** exhibit nearly identical spectra featuring two quadrupole doublets with isomer shifts lower than that of the diiron complex **3** (Table 2). In the case of  $Fe_2Mn$  cluster **5**, the Mössbauer spectrum (parameters  $\delta, |ΔE_Q|$  (mm/s): component 1 (52%) 0.58, 1.30; component 2 (48%) 0.35, 1.77; Figure 4b.1) is consistent with the presence of two inequivalent Fe centers and is demonstrative of a site-isolated insertion of a single Mn center into the  $Fe_2$  complex **3**. Site-isolated insertion of a single Fe into dimanganese

**Table 2.** Zero-field  $^{57}Fe$  Mössbauer Parameters for Fe Containing Compounds

compound	$\delta$ (mm/s)	$ ΔE_Q $ (mm/s)	%
$(^{tbs}L)Fe_3(THF)$ ( <b>1</b> )	0.89	1.69	24
	0.49	1.51	35
	0.50	1.89	41
$(^{tbs}L)Fe_2$ ( <b>3</b> )	0.67	2.18	39
	0.68	1.57	61
$(^{tbs}L)Fe_2Mn(THF)$ ( <b>5</b> )	0.35	1.77	48
	0.58	1.30	52
$(^{tbs}L)Mn_xFe_{3-x}(THF)$ ( <b>6</b> )	0.33	1.85	48
	0.57	1.31	52

compound **4** would result in a Mössbauer spectrum exhibiting a single quadrupole doublet; however, the spectrum of crystalline **6** features two quadrupole doublets (parameters  $\delta, |ΔE_Q|$  (mm/s): component 1 (52%) 0.57, 1.31; component 2 (48%) 0.33, 1.85) (Figure 4b.2). While the Mössbauer spectra of cluster **6** could be indicative of a mixture of clusters (e.g.,  $Mn_2Fe$  and  $Fe_2Mn$ ), the two quadrupole doublets could also arise from a single compositional species (i.e.,  $Mn_2Fe$ ) where the Fe atom occupies more than one geometrically distinct site.

The spectroscopic data discussed thus far for  $Fe_2Mn$  cluster **5** is consistent with isolation of a substitutionally homogeneous material  $(^{tbs}L)Fe_2Mn(THF)$ . However, the data associated with compound **6** is less clear and could either be attributed to a mixture of compositions or a homogeneous material where the Fe is located in multiple metal positions. Combustion analysis on crystalline **6** is consistent with  $(^{tbs}L)Mn_xFe_3(THF)$  and  $(^{tbs}L)Fe_2Mn(THF)$  within the error of the experiment. Therefore, X-ray fluorescence spectroscopy was used as a means of bulk elemental analysis of the metal composition in the crystalline material. X-ray fluorescence spectra of mixed-metal compounds **5** and **6** exhibited both Fe and Mn  $K\alpha$  and  $K\beta$  emission lines, where the Fe  $K\alpha$  and the Mn  $K\beta$  overlap (Figure 4c). The superposition of the Fe  $K\alpha$  and Mn  $K\beta$  emission lines for clusters **5** resulted in Fe:Mn ratios of 2.3:1 (70% Fe content) and 1.8:1 (64% Fe content) from the two samples collected (Figure 4c), which are consistent with what would be expected for a substitutionally homogeneous  $Fe_2Mn$  cluster. However, this is not the case for species **6**, which was found to have a Fe:Mn ratio lower than expected (1:1.3 and



1:1.2 from the two samples collected, 45 and 47% Fe content, respectively) (Figure 4c), indicating that **6** contains >33% iron.

Therefore, we used anomalous scattering to determine the relative metal occupancies at the three unique sites within the mixed-metal clusters. To better understand the role ancillary ligands (coordinated solvent molecule, Scheme 1 *vide supra*) play in the selectivity of the metal substitution reaction, we conducted the synthesis of Mn<sub>2</sub>Fe cluster in the presence of pyridine (py) (**7**, *vide supra*) and grew crystals of the material for anomalous scattering experiments.

**3.2. Anomalous X-Ray Scattering.** While conventional single-crystal X-ray diffraction provides information regarding the identity and connectivity of the atoms, this method cannot distinguish between two metals of nearly the same atomic number. Anomalous X-ray scattering is a technique that allows for differentiation between metal atoms with similar atomic weights.<sup>27</sup> At an incident radiation wavelength close to the absorption edge of a metal center, the atomic scattering factors for elements with similar atomic numbers become more distinct. The atomic scattering factor for a given element is expressed by:

$$f = f^{\circ} + f' + if''$$

where  $f^{\circ}$  is the scattering factor of the unperturbed atom (proportional to the atomic number of the element), and  $f'$  and  $f''$  are the real and imaginary components, respectively, of the anomalous scattering term, which vary as a function of the X-ray wavelength energy.<sup>27</sup> Normal single crystal X-ray diffraction data is collected at a wavelength of incident X-rays away from the absorption edges of the constituent elements, where  $f \approx f^{\circ}$ . At energies close to the absorption edge of an atom M, the anomalous dispersion terms become more significant in the overall atomic scattering factor ( $f$ ) of that atom, which affects the diffraction intensity associated with M. This method has been used to differentiate metal centers in solid-state materials by both powder<sup>28</sup> and single-crystal diffraction,<sup>23,29</sup> as well as being utilized in protein crystallography.<sup>30,31</sup> We have employed anomalous X-ray scattering as a method for site-specific elemental analysis to elucidate the elemental composition at each of the three metal-binding sites in our trinuclear complexes. Table 3 summarizes the synchrotron data sets measured at different wavelengths. The real ( $f'$ ) and imaginary ( $f''$ ) components of anomalous scattering are theoretical values for pure Fe and Mn metal.<sup>20</sup> While the anomalous scattering terms will vary with charge and

**Table 3. Synchrotron Data Sets Measured at Different Wavelengths: Anomalous Dispersion Terms  $f'$  and  $f''$  Are for Pure Fe<sup>0</sup> and Mn<sup>0</sup> Metal<sup>20</sup>**

data set	$\lambda$ (Å)	energy (KeV)	Fe $f', f''$ ( $e^-$ )	Mn $f', f''$ ( $e^-$ )	$ \Delta f ^a$
1a	0.44280	28.000	0.220, 0.350	0.200, 0.300	0.070
1b	0.49594	25.000	0.255, 0.434	0.234, 0.373	0.082
2	1.91068	6.489	-2.166, 0.552	-4.594, 0.469	2.511
3	1.89607	6.539	-2.241, 0.544	-9.901, 0.462	7.742
4	1.88169	6.589	-2.324, 0.537	-4.486, 3.904	1.205
5a	1.75565	7.062	-4.646, 0.474	-1.731, 3.452	5.893
5b	1.75070	7.082	-5.183, 0.471	-1.686, 3.437	6.463
6	1.74331	7.112	-9.812, 0.468	-1.622, 3.414	11.14
7	1.73114	7.162	-4.547, 3.896	-1.522, 3.377	2.506

$$^a|\Delta f| = |[f'(Mn)+f''(Mn)]-[f'(Fe)+f''(Fe)]|.$$

coordination environment, theoretical values of pure metals have been used in the past with success at accurately determining metal occupancies at mixed-metal sites.<sup>23</sup> In all cases, a reference data set was collected away from any metal absorption edges (data set 1a or 1b). Compound **5** was measured at the absorption edge of Mn and Fe (data set 3 and 6, respectively). Additional data sets were collected above and/or below the absorption edge for compounds **6** and **7**.

Electron density difference maps provide a means to visualize the anomalous scattering data obtained at the absorption edges. Dispersive difference Fourier 2D maps of the trimetal plane were generated for compounds **5**, **6**, and **7** at both the Mn and Fe absorption edges (Figure 5). Dispersive difference maps at the Mn absorption edge were generated using the coefficients  $F_{Mn} - F_{ref}$  where  $F_{Mn}$  is data set 3 and  $F_{ref}$  is one of the two reference data sets 1a or 1b, which was previously refined with all Fe metal centers. Likewise, the coefficients  $F_{Fe} - F_{ref}$  ( $F_{Fe}$  = data set 6, reference structure previously refined with all Mn metal centers) were used to create the difference maps at the Fe absorption edge. The difference map at the Mn absorption edge (data set 3) of (t<sup>bs</sup>L)Fe<sub>2</sub>Mn(THF) **5** (Figure 5a) features an electron density hole at M1 ( $-3.78 e^-/\text{Å}^3$ ), indicating incorporation of Mn into that binding site. At the Fe absorption edge (data set 6) of compound **5** the difference map shows deep electron density holes at positions M2 and M3 with energies  $-5.31 e^-/\text{Å}^3$  and  $-4.58 e^-/\text{Å}^3$  respectively, indicative of Fe incorporation into those metal sites (Figure 5b). The difference in electron density at M2 and M3 could either be a result of slight atomic movements/changes in unit cell size upon irradiation of X-rays at different wavelengths (the 2D plane at the Fe absorption edge may not contain the absolute centers, location of lowest electron density, of all three metals) or the difference may indicate that the two metal positions are not equivalently occupied with Fe.<sup>23</sup> Free refinement of the data at the Mn absorption edge results in statistically equivalent occupancies at positions M2 and M3 (M2, 95.9(5)%; M3, 96.2(6)%), which supports equivalent Fe occupancy at M2 and M3 (Supporting Information Table S7). The anomalous difference Fourier 2D maps of the trimetal plane of compound **5** in conjunction with the free-refinement of the metal centers at the metal absorption edges is demonstrative of site-isolated insertion of a single divalent Mn center into the cluster (M1) which is bound to the solvent molecule THF.

Electron density difference maps of **6** and **7** (Figure 5c–e) are consistent with M1 fully occupied by Mn and M3 fully occupied by Fe, showing deep electron density holes at the Mn and Fe absorption edges, respectively, at those metal sites (at Mn absorption edge of **6**: M1 =  $-3.62 e^-/\text{Å}^3$ ; **7**: M1 =  $-6.99 e^-/\text{Å}^3$ ; at Fe absorption edge of **6**: M3 =  $-5.03 e^-/\text{Å}^3$ ; **7**: M3 =  $-3.71 e^-/\text{Å}^3$ ). The data suggest M2 in both **6** and **7** is a compositional mixture, occupied by both Fe and Mn, as indicated by the observation of weaker negative electron density at both absorption edges (at Mn absorption edge of **7**:  $-3.08 e^-/\text{Å}^3$ ; at Fe absorption edge of **6**: M2 =  $-0.07 e^-/\text{Å}^3$ ; **7**:  $-0.71 e^-/\text{Å}^3$ ).

Anomalous structure refinements of **5**, **6**, and **7** were conducted using the SHELX program package.<sup>19</sup> A disorder model was utilized to determine the extent of compositional mixing at position M2 in **6** and **7**. The results of the disorder refinements at various wavelengths for compounds **6** and **7** are summarized in Table 4. While the disorder refinement indicates that both Fe and Mn occupy position M2 in **6** and **7** in nearly a 1:1 ratio, the disorder model did not produce consistent results

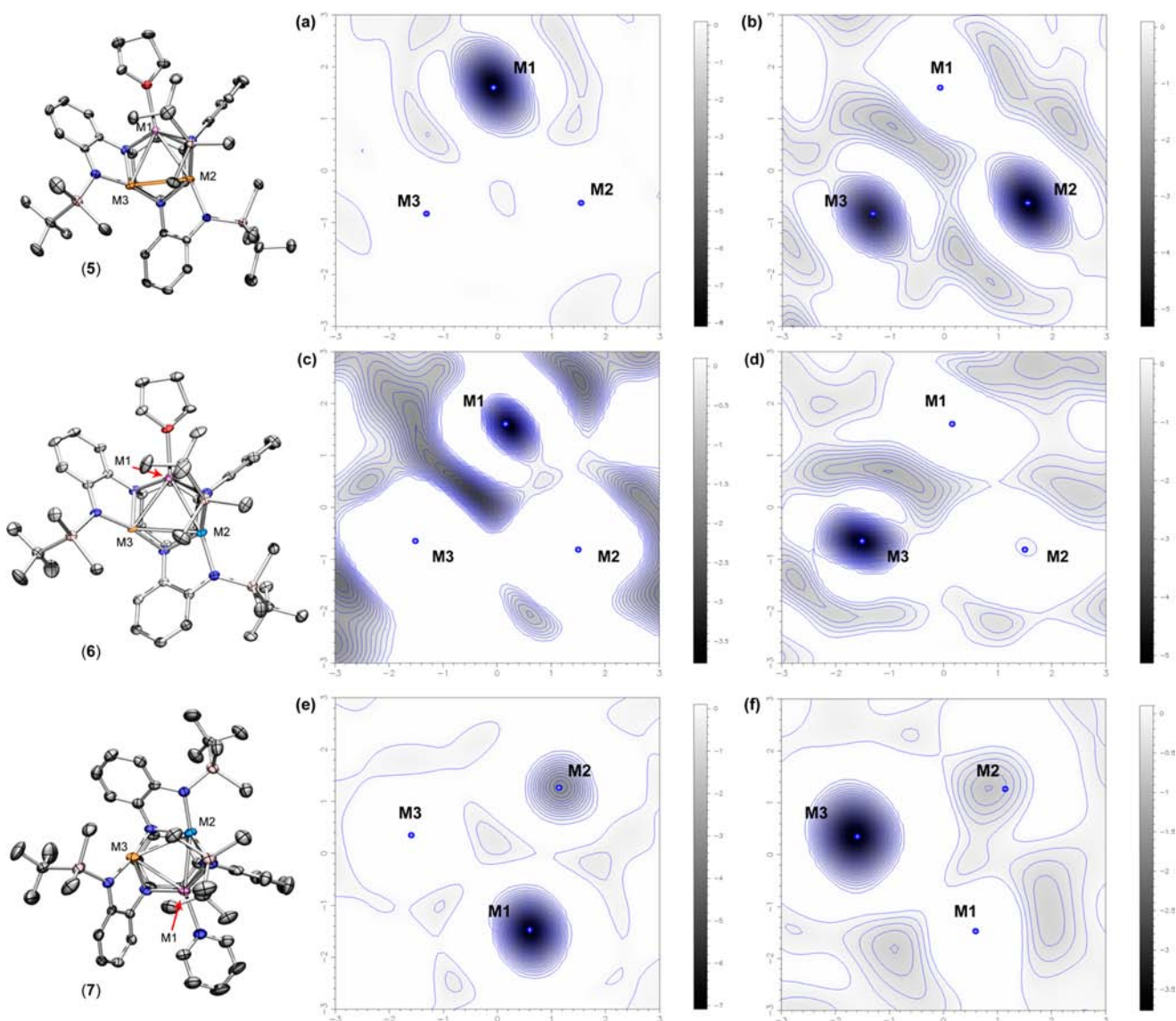


**Figure 5.** Anomalous difference Fourier maps at the Mn and Fe absorption edges of compounds  $(^{10}\text{L})\text{Fe}_2\text{Mn}(\text{THF})$  (5) (a, b), 6 (c, d), and 7 (e, f). Maps (a), (c), and (e) were calculated with data set 3 (at the Mn absorption edge) and maps (b), (d), and (f) were calculated with data set 6 (at the Fe absorption edge).

**Table 4. Refined Fe Occupancies (%) with SHELXL for 6 and 7**

metal site	data set 2	data set 3	data set 4	data set 5	data set 6	data set 7
Compound 6				5a		
M1	0 <sup>a</sup>	6(2)	0 <sup>a</sup>	10(3)	5(2)	29(7)
M2	53(3)	59(1)	54(3)	58(3)	44(2)	84(7)
M3	100 <sup>b</sup>	100(1)	100 <sup>b</sup>	100 <sup>b</sup>	66(2)	100 <sup>b</sup>
Compound 7				5b		
M1		15(2)		0 <sup>a</sup>	12(3)	
M2		41(3)		41(3)	36(3)	
M3		100 <sup>b</sup>		100 <sup>b</sup>	81(3)	

<sup>a</sup>Disorder model results in >100% occupancy Mn at M1, therefore refined as 100% Mn. <sup>b</sup>Disorder model results in >100% occupancy Fe at M3, therefore refined as 100% Fe.

at the different wavelengths, due to variability associated with the anomalous dispersion terms (*vide supra*).<sup>23,29</sup>

To assess the relative errors in percent occupancy associated with the anomalous dispersion terms, the values of  $f'$  and  $f''$  were varied for compound 6 and the percent occupancies at the different metal sites were calculated.<sup>28</sup> We found that data sets 3, 4, 6, and 7 showed high errors associated with varying  $f'$  and  $f''$  values (Supporting Information Table S9). The  $f'$  and  $f''$  values at the absorption edges (data sets 3 and 6) are most sensitive to variation in energy and are therefore difficult to approximate at the absorption edge.<sup>29</sup> The data set after the highest absorption edge (Fe, data set 7) is less accurate because the  $f''$  values for the two metal centers are closest at this energy, lowering the  $\Delta f$  value and making it more difficult to discern between the two metal centers.<sup>23</sup> Similarly, the data set following the Mn absorption edge (data set 4) is less accurate because the Mn  $f''$  is highest at this energy, also lowering the  $\Delta f$  value. Therefore, only data sets 2 and 5 were utilized to determine the percent occupancies of the metal positions in 6, while data set 5 was used to determine the percent occupancies of the metal positions in 7.



Using the results of the disorder model at data sets 2 and 5, we found the average percent occupancies of Fe for compound **6** to be: M1 = 5(3), M2 = 56(4), and M3 = 100 (Table 4). While the disorder model predicts that a small amount of inclusion of Fe has occurred at M1, based on the fact that no negative electron density hole was observed at that position in the electron density map at the Fe absorption edge and that the zero-field  $^{57}\text{Fe}$  Mössbauer spectrum contains only two quadrupole doublets, we have assigned M1 as a fully occupied Mn site, resulting in a 1.3:1 mixture of  $(^{\text{tbs}}\text{L})\text{Fe}_2\text{Mn}(\text{THF})$ :  $(^{\text{tbs}}\text{L})\text{Mn}_2\text{Fe}(\text{THF})$  based on crystal structure analysis. Compound **7** has a similar composition to **6**, with Fe percent occupancies of M1 = 0, M2 = 41(3), and M3 = 100 (data set 5) resulting in a 1:1.4 mixture of  $(^{\text{tbs}}\text{L})\text{Fe}_2\text{Mn}(\text{py})$ :  $(^{\text{tbs}}\text{L})\text{Mn}_2\text{Fe}(\text{py})$  based on anomalous crystal structure analysis.

#### 4. DISCUSSION

Substitution of metal centers to generate heteropolynuclear species has been used as a method of accomplishing changes in both reactivity and electronic structure of polynuclear clusters. Through this study we aimed to adapt our synthetic approach to include bimetallic trinuclear species, which would allow us to investigate changes in M–M interactions upon metal substitution in a stepwise fashion. Utilizing homodinuclear compounds as synthons, we targeted the synthesis of mixed Fe/Mn clusters supported within a hexaanilide-based ligand platform (Scheme 1, *vide supra*). Our strategy resulted in the synthesis of a discrete  $\text{Fe}_2\text{Mn}$  complex  $(^{\text{tbs}}\text{L})\text{Fe}_2\text{Mn}(\text{THF})$  (**5**) (Scheme 2). Spectroscopic techniques including  $^1\text{H}$  NMR,

as  $^1\text{H}$  NMR of **6** was also consistent with a mixture of  $\text{Fe}_2\text{Mn}$  and  $\text{Mn}_2\text{Fe}$  species, containing two quadrupole doublets in the Mössbauer and more than double the number of resonances in the  $^1\text{H}$  NMR (including all of the resonances) observed for  $\text{Fe}_2\text{Mn}$  cluster **5**.

While traditional X-ray crystallography established connectivity within the bimetallic trinuclear clusters, anomalous X-ray scattering was employed to differentiate the elemental compositions within the clusters. Anomalous X-ray scattering corroborates both bond metrics obtained by single crystal X-ray analysis of  $\text{Fe}_2\text{Mn}$  cluster (**5**) as well as the spectroscopic data obtained for **5**, indicating site-isolated Mn insertion into the diiron synthon **3** with Mn bound to the THF molecule (Scheme 2).

Both electron density difference maps and data refinement obtained from anomalous scattering measurements confirmed the presence of a mixture of the two species  $(^{\text{tbs}}\text{L})\text{Fe}_2\text{Mn}(\text{E})$  and  $(^{\text{tbs}}\text{L})\text{Mn}_2\text{Fe}(\text{E})$  (where E = THF or py) in the crystal structure of **6** and **7**. In both **6** and **7**, M1 is fully occupied by Mn and M3 is fully occupied by Fe, while the only mixed-metal site in the solid-state was determined to be M2 (**6**: 56(4)% Fe; **7**: 41(3)% Fe) (Scheme 2).

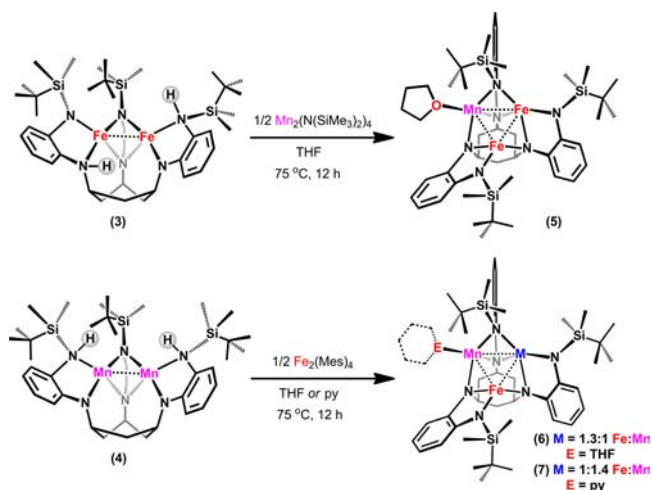
Ligand or metal lability allows for the Mn atoms to be displaced by divalent Fe centers. Monitoring the reaction of  $\text{Mn}_2$  **4** with 0.5 equivalent  $\text{Fe}_2\text{Mes}_4$  by  $^1\text{H}$  NMR spectroscopy, we see immediate formation of the resonances associated with  $\text{Fe}_2\text{Mn}$  and  $\text{Mn}_2\text{Fe}$ . By  $^1\text{H}$  NMR, we observe that upon addition of 1–2 equivalents of  $\text{Fe}_2\text{Mes}_4$  to  $\text{Mn}_2$  complex **4**, we see the disappearance of the peaks associated with  $\text{Mn}_2\text{Fe}$  cluster to yield a paramagnetic  $^1\text{H}$  NMR that predominantly contains the resonances associated with  $\text{Fe}_2\text{Mn}$  cluster **5** (Supporting Information Figure S10). The ability to isolate  $\text{Fe}_2\text{Mn}$  complex **5** likely results due to a slight thermodynamic preference over the  $\text{Mn}_2\text{Fe}$  species under the reaction conditions employed. Metal atom exchange has been previously observed in trinuclear clusters supported by hexaanilide based ligand platforms to generate mixed Fe/Co systems at room temperature.<sup>12</sup>

Although we present the Fe and Mn ions with an unbiased ligand scaffold comprised of three OPDA subunits, each metal site has a unique coordination environment in the solid-state as observed crystallographically. The results herein demonstrate that the differences in coordination environment at each metal position of these clusters have an effect on whether Fe or Mn preferentially binds in each unique pocket. In all three mixed-metal complexes, Fe ( $d^6$ ) fully occupies the M3 position, which is 3-coordinate, bound to two internal alkyl aryl anilides and one peripheral anilide ligand moiety. Mn has a lower  $d$ -electron count ( $d^5$ ) relative to Fe and prefers the 4-coordinate positions M1 and M2. The ligated solvent appears to have little to no effect on the ratio of metal occupancy within the clusters, as evidenced by the nearly equivalent Fe:Mn ratios for **6** and **7**, as well as the unique Mn position (M1) binds exogenous solvent in both species.

#### 5. CONCLUSIONS

The polynucleating ligand platform  $^{\text{tbs}}\text{LH}_6$  was selected as the template for the synthesis of bimetallic trinuclear clusters. By accessing the dinuclear metal species  $(^{\text{tbs}}\text{LH}_2)_2\text{M}_2$  (M = Fe, Mn), we envisioned the synthesis of discrete metal platforms from  $\text{Mn}_3$  to  $\text{Fe}_3$  in single metal-substitution steps. While the ligand  $^{\text{tbs}}\text{LH}_6$  presents each metal center with an identical binding pocket comprised of an OPDA, the resulting trinuclear

**Scheme 2. Results of Bimetallic Trinuclear Syntheses Summarized<sup>a</sup>**



<sup>a</sup>Fe:Mn content in **6** and **7** based on anomalous scattering experiments.

Mössbauer, and X-ray crystallography were all consistent with isolation of a substitutionally homogeneous material, while X-ray fluorescence spectroscopy of the bulk crystalline material established that the Fe:Mn content was 2:1. Encouraged by this result, we attempted to access a similar  $\text{Mn}_2\text{Fe}$  cluster in an analogous fashion. Unlike **5**, each of the spectroscopies employed indicate an oversubstitution of iron into the cluster. X-ray fluorescence spectroscopy of compound **6** indicated more Fe incorporation into the crystalline material than expected ( $46 \pm 1\%$  Fe content). Both  $^{57}\text{Fe}$  Mössbauer spectroscopy as well

clusters exhibit  $C_1$ -symmetry in solution and the solid-state, indicating that each metal within the cluster possesses a unique coordination environment. The asymmetric binding of the ligand about the trinuclear core permits the unambiguous assignment of each metal binding site through a suite of spectroscopic techniques. The thermodynamic bimetallic trinuclear product ( $^{tbs}L$ )Fe<sub>2</sub>Mn(THF) was accessed cleanly as a substitutionally homogeneous material, where the Mn insertion is site-isolated. During attempts at the synthesis of Mn<sub>2</sub>Fe clusters (**6** and **7**), we observe both the formation of the kinetic product ( $^{tbs}L$ )Mn<sub>2</sub>Fe(THF) as well as the thermodynamic product, ( $^{tbs}L$ )Fe<sub>2</sub>Mn(THF), immediately following mixing ( $^{tbs}LH_2$ )Mn<sub>2</sub> with Fe<sub>2</sub>(Mes)<sub>4</sub>. This initial study has provided a direct synthetic approach to access bimetallic trinuclear clusters supported by the sterically hindered hexaanilide ligand platform  $^{tbs}LH_6$ . Research is currently underway to extend this methodology to include other redox-active and redox-inactive metal atoms into polynuclear clusters and to investigate changes in both ensemble electronic structures as well as reactivity profiles.

## ■ ASSOCIATED CONTENT

### ■ Supporting Information

Detailed spectroscopic and crystal structure data for all new compounds. This material is available free of charge via the Internet at <http://pubs.acs.org>.

## ■ AUTHOR INFORMATION

### Corresponding Author

betley@chemistry.harvard.edu

### Notes

The authors declare no competing financial interest.

## ■ ACKNOWLEDGMENTS

We thank Harvard University, NIH (GM 098395), DOE (DE-SC0008313) for financial support, Prof. R. H. Holm for the generous use of his Mössbauer spectrometer, the George W. Merck Fellowship (T.A.B), the Novartis Graduate Fellowship in Chemical Sciences for Minorities and Women and the Marie Hong fellowship (T.M.P.), the NIH Ruth L. Kirschstein NRSA fellowship (A.R.F.), and the CONACTY and Fundación México en Harvard A. C. (R.H.S.). ChemMatCARS Sector 15 is principally supported by the National Science Foundation/Department of Energy under grant number NSF/CHE-0822838. Use of the Advanced Photon Source was supported by the U.S. Department of Energy, Office of Science, Office of Basic Energy Sciences, under Contract No. DE-AC02-06CH11357.

## ■ REFERENCES

- (1) (a) Burgess, B. K.; Lowe, D. J. *Chem. Rev.* **1996**, *96*, 2983–3012. (b) Howard, J. B.; Rees, D. C. *Chem. Rev.* **1996**, *96*, 2965–2982. (c) Dos Santos, P. C.; Igarashi, R. Y.; Lee, J.-I.; Hoffman, B. M.; Seefeldt, L. C.; Dean, D. R. *Acc. Chem. Res.* **2005**, *38*, 208–214. (d) Hoffman, B. M.; Lukoyanov, D.; Dean, D. R.; Seefeldt, L. C. *Acc. Chem. Res.* **2009**, *42*, 609–619. (e) Eady, R. R. *Chem. Rev.* **1996**, *96*, 3013–3030. (f) Hu, Y.; Lee, C. C.; Ribbe, M. W. *Dalton Trans.* **2012**, *41*, 1118–1127.
- (2) (a) Jiang, W.; Yun, D.; Saleh, L.; Barr, E. W.; Xing, G.; Hoffart, L. M.; Maslak, M.-A.; Krebs, C.; Bollinger, M., Jr. *Science* **2007**, *316*, 1188–1191. (b) Younker, J. M.; Krest, C. M.; Jiang, W.; Krebs, C.; Bollinger, J. M., Jr.; Green, M. T. *J. Am. Chem. Soc.* **2008**, *130*, 15022–

15027. (c) Bollinger, J. M., Jr.; Jiang, W.; Green, M. T.; Krebs, C. *Curr. Opin. Struct. Biol.* **2008**, *18*, 650–657.

- (3) (a) Sinfelt, J. H. *Bimetallic Catalysts. Discoveries, Concepts, and Applications*; Wiley: New York, 1983. (b) Sinfelt, J. H. *Acc. Chem. Res.* **1977**, *10*, 15–20. (c) Ponc, V. *Appl. Catal., A* **2001**, *222*, 31–45. (d) Thomas, J. M.; Raja, R.; Johnson, B. F. G.; Hermans, S.; Jones, M. D.; Khimyak, T. *Ind. Eng. Chem. Res.* **2003**, *42*, 1563–1570. (e) Gladys, M. J.; Inderwildi, O. R.; Karakatsani, S.; Fiorin, V.; Held, G. *J. Phys. Chem. C* **2008**, *112*, 6422–6429. (f) Santo, V. D.; Gallo, A.; Naldoni, A.; Guidotti, M.; Psaro, R. *Catal. Today* **2012**, *197*, 190–205. (h) Calderone, V. R.; Shiju, N. R.; Ferré, D. C.; Rothenberg, G. *Green Chem.* **2011**, *13*, 1950–2216. (g) Arai, H.; Mitsuishi, K.; Seiyama, T. *Chem. Lett.* **1984**, 1291–1294.

- (4) (a) Clegg, W.; Elsegood, M. R. J.; Errington, J.; Havelock, J. J. *Chem. Soc., Dalton Trans.* **1996**, 681–690. (b) Wei, Y.; Lu, M.; Cheung, C. F.-c.; Barnes, C. L.; Peng, Z. *Inorg. Chem.* **2001**, *40*, 5489–5490.

- (5) (a) Ciurli, S.; Ross, P. K.; Scott, M. J.; Yu, S.-B.; Holm, R. H. *J. Am. Chem. Soc.* **1992**, *114*, 5415–5423. (b) Zhou, J.; Scott, M. J.; Hu, Z.; Peng, G.; Münck, E.; Holm, R. H. *J. Am. Chem. Soc.* **1992**, *114*, 10843–10854.

- (6) Slaughter, L. M.; Wolczanski, P. T. *Chem. Commun.* **1997**, 2109–2110.

- (7) (a) Hung, S. Y.-W.; Wong, W.-T. *Chem. Commun.* **1997**, 2099–2100. (b) Adams, R. D.; Barnard, T. S.; Li, Z.; Wu, W.; Yamamoto, J. H. *J. Am. Chem. Soc.* **1994**, *116*, 9103–9113.

- (8) Tulskey, E. G.; Long, J. R. *Inorg. Chem.* **2001**, *40*, 6990–7002.

- (9) (a) Holm, R. H. *Adv. Inorg. Chem.* **1992**, *38*, 1–71. (b) Johnson, M. K.; Duderstadt, R. E.; Duin, E. C. *Adv. Inorg. Chem.* **1999**, *47*, 1–82. (c) Hernandez-Molina, R.; Sokolov, M. N.; Sykes, A. G. *Acc. Chem. Res.* **2001**, *34*, 223–230.

- (10) (a) Clerac, R.; Cotton, F. A.; Dunbar, K. R.; Murillo, C. A.; Wang, X. *Chem. Chem.* **2001**, *40*, 420–426. (b) Nippe, M.; Berry, J. F. *J. Am. Chem. Soc.* **2007**, *129*, 12684–12685.

- (11) (a) Pilkington, N. H.; Robson, R. *Aust. J. Chem.* **1970**, *23*, 2225–2236. (b) Beissel, T.; Birkelback, F.; Bill, E.; Glaser, T.; Kesting, F.; Krebs, C.; Weyhermüller, T.; Wieghardt, K.; Butzlaff, C.; Trautwein, A. X. *J. Am. Chem. Soc.* **1996**, *118*, 12376–12390. (c) Glaser, T.; Kesting, F.; Bill, E.; Weyhermüller, T.; Klaucke, W.; Wieghardt, K. *Inorg. Chem.* **1999**, *38*, 722. (d) Akilne, S.; Taniguchi, T.; Nabeshima, T. *Inorg. Chem.* **2008**, *47*, 3255–3264. (e) Akilne, S.; Taniguchi, T.; Nabeshima, T. *Inorg. Chem.* **2008**, *47*, 3255–3264. (f) Greenwood, B. P.; Forman, S. I.; Rowe, G. T.; Chen, C.-H.; Foxman, B. M.; Thomas, C. M. *Inorg. Chem.* **2009**, *48*, 6251–6260. (g) Rudd, P. A.; Liu, S.; Gagliardi, L.; Young, V. G., Jr.; Lu, C. C. *J. Am. Chem. Soc.* **2011**, *133*, 20724–20727.

- (12) Eames, E. V.; Hernández Sánchez, R.; Betley, T. A. *Inorg. Chem.* **2013**, *52*, 5006–5012.

- (13) (a) Zhao, Q.; Betley, T. A. *Angew. Chem., Int. Ed.* **2011**, *50*, 709–712. (b) Fout, A. R.; Zhao, Q.; Xiao, D. J.; Betley, T. A. *J. Am. Chem. Soc.* **2011**, *133*, 16750–16753. (c) Eames, E. V.; Harris, T. D.; Betley, T. A. *Chem. Sci.* **2012**, *3*, 407–415. (d) Eames, E. V.; Betley, T. A. *Inorg. Chem.* **2012**, *51*, 10274–10278.

- (14) (a) Powers, T. M.; Fout, A. R.; Zhao, S.-L.; Betley, T. A. *J. Am. Chem. Soc.* **2011**, *133*, 3336–3338. (b) Powers, T. M.; Betley, T. A. *J. Am. Chem. Soc.* **2013**, *135*, 12289–12296.

- (15) Klose, A.; Solari, E.; Floriani, C.; Chiesi-Villa, A.; Rizzoli, C.; Re, N. *J. Am. Chem. Soc.* **1994**, *116*, 9123–9135.

- (16) Solari, E.; Musso, F.; Gallo, E.; Floriani, C.; Re, N.; Chiesi-Villa, A.; Rizzoli, C. *Organometallics* **1995**, *14*, 2265–2276.

- (17) Bradley, D. C.; Hursthouse, M. B.; Malik, K. M. A.; Moseler, R. *Transition Met. Chem.* **1978**, *3*, 253.

- (18) Bruker AXS. *Apex II*; Bruker AXS: Madison, WI, 2009.

- (19) Sheldrick, G. M. *Acta Crystallogr.* **2010**, *D66*, 479–485.

- (20) Real ( $f'$ ) and imaginary ( $f''$ ) components were obtained from Kissel, L.; Pratt, R. H. *Acta Crystallogr.* **1990**, *A46*, 170–175 unless otherwise noted.

- (21) Farrugia, L. J. *J. Appl. Crystallogr.* **1999**, *32*, 837–838.

- (22) Rohlicek, J.; Husak, M. *J. Appl. Crystallogr.* **2007**, *40*, 600–601.

(23) Helliwell, M.; Helliwell, J. R.; Kaucic, V.; Logar, N. Z.; Teat, S. J.; Warren, J. E.; Dodson, E. J. *Acta Crystallogr.* **2010**, *B66*, 345–357.

(24) Fout, A. R.; Xiao, D. J.; Zhao, Q.; Harris, T. D.; King, E. R.; Eames, E. V.; Zheng, S.-L.; Betley, T. A. *Inorg. Chem.* **2012**, *51*, 10290–10299.

(25) While mixed-metal py ligated cluster **7** is not discussed in section 3.1, it has been fully characterized by the spectroscopic methods described herein and exhibits similar spectroscopic features compared to THF ligated mixed-metal cluster **6** (see Experimental section).

(26) Murphy, D. M. EPR (Electron Paramagnetic Resonance) Spectroscopy of Polycrystalline Oxide Systems. In *Metal Oxide Catalysis*; Jackson, S. D., Hargreaves, J. S. J., Eds.; Wiley-VCH: Weinheim, 2009.

(27) Waseda, Y. *Anomalous X-ray Scattering for Materials Characterization: Atomic-Scale Structure Determination*; Springer: Berlin, 2002.

(28) (a) Battle, P. D.; Blundell, S. J.; Coldea, A. I.; Cussen, E. J.; Rosseinsky, M. J.; Singleton, J.; Spring, L. E.; Vente, J. F. *J. Mater. Chem.* **2001**, *11*, 160–167. (b) Zhang, Y.; Wilkinson, A. P.; Nolas, G. S.; Lee, P. L.; Hodges, J. P. *J. Appl. Crystallogr.* **2003**, *36*, 1182–1189. (c) Zhang, Y.; Wilkinson, A. P.; Lee, P. L.; Shastri, S. D.; Shu, D.; Chung, D.-Y.; Kanatzidis, M. G. *J. Appl. Crystallogr.* **2005**, *38*, 433–441.

(29) (a) Wulf, R. *Acta Crystallogr.* **1990**, *A46*, 681–688. (b) Freedman, D. E.; Han, T. H.; Prodi, A.; Müller, P.; Huang, Q.-Z.; Chen, Y.-S.; Webb, S. M.; Lee, Y. S.; McQueen, T. M.; Nocera, D. G. *J. Am. Chem. Soc.* **2010**, *132*, 16185–16190. (c) Zhang, X.; Huang, D.; Chen, Y.-S.; Holm, R. H. *Inorg. Chem.* **2012**, *51*, 11017–11029. (d) Zall, C. M.; Clouston, L. J.; Young, V. G., Jr.; Ding, K.; Kim, H. J.; Zhrebetsky, D.; Chen, Y.-S.; Bill, E.; Gagliardi, L.; Lu, C. C. *Inorg. Chem.* **2013**, *52*, 9216–9228.

(30) Dauter, M.; Dauter, Z. Phase Determination Using Halide Ions. In *Macromolecular Crystallography Protocols. Vol. 2: Structure Determination*; Doublé, S., Ed.; Humana Press: Totowa, NJ, 2007; Vol. 364, p 149.

(31) Klabunde, K. J. *Free Atoms, Clusters, and Nanoscale Particles*; Academic Press, Inc: San Diego, 1994.